HHS Public Access

Author manuscript

Nat Struct Mol Biol. Author manuscript; available in PMC 2020 March 05.

Published in final edited form as:

Nat Struct Mol Biol. 2019 September ; 26(9): 802–807. doi:10.1038/s41594-019-0274-2.

Resolution of angstrom-scale protein-conformational changes by analyzing fluorescence anisotropy

John H. Lewis, **Zhe Lu**[1]

Department of Physiology, Perelman School of Medicine, University of Pennsylvania, Philadelphia, PA 19104

Summary

Conformational changes within typical protein molecules are rapid and small, making their quantitative resolution challenging. These changes generally involve rotational motions, and may thus be resolved by determining changes in the orientation of a fluorescent label that assumes a unique orientation in each conformation. Here, by analyzing fluorescence intensities collected using a polarization microscope at a rate of 50 frames per second, we can follow the changes of 10 to 16° in the orientation of a single bifunctional rhodamine molecule attached to an RCK domain of the MthK channel, and thus the transitions among its three conformational states, with effective standard deviation (σ) of 2 to 5°. Based on available crystal structures, the position of the fluorophore's center differ by 3.4 to 8.1 Å among the states. Thus, the present approach allows the resolution of protein-conformational changes involving angstrom-scale displacements.

Introduction

Understanding the energetic and kinetic mechanisms of conformational changes of a protein, and relating them to known atomic structures of its conformational states require the capability to resolve and monitor the changes of its spatial characteristics, which are unique to individual conformational states, with adequate spatial and temporal resolutions. Conformational changes of protein molecules may occur temporally and spatially on millisecond and angstrom scales. On these temporal and spatial scales, resolution of multi-state protein-conformational changes at a single-protein-molecule level by measuring distance changes remains extremely challenging. However, protein conformational changes generally involve rotational motions of their domains, in which secondary structure elements such as α-helices might adopt unique spatial orientations among individual conformational states. In such cases, resolving the conformational states of a protein could be reduced to resolving the spatial orientation of a single suitable structural element with unique orientation in each state.

[1]Corresponding author.

Author Contributions

J.H.L and Z.L. designed the study; J.H.L assembled the polarization microscope, performed experiments, developed analytical tools, and analyzed the data, with the input from Z.L.; J.H.L. and Z.L. interpreted the results and wrote the manuscript.

Competing Interests

There are no competing interests.

In a spherical coordinate system, the orientation of an object, here represented by a vector, can be defined by three inherently nonequivalent parameters, namely, the length (R) and two angles: inclination (θ, from 0° to 180°) and rotation (φ, from 0° to 360°) (Fig. 1a; all notations are defined in Supplementary Note 1). The two angles contain the full information regarding spatial orientation, independent of R. Thus, in order to track orientation changes and relate those tracked conformations to known protein structures, monitoring θ and φ alone should suffice. The estimated median radius of proteins is about 20 Å[1, 2]. A rotation of 5 – 10° of a site 20 Å away from the origin would lead to a 1.7 – 3.5 Å change in the chord distance. Thus, the capability to resolve angle changes on this scale would in principle allow the study of atomic-scale conformational changes in typical proteins.

One approach to track changes in orientation of a protein region is to monitor the orientation of an attached fluorophore (Fig. 1a) using a polarization microscope. The resolution of the changes in a fluorophore's emission-polarization changes (independently of wavelength) is limited in practice by the signal-to-noise ratio (SNR) and cannot exceed what is predicted from the so-called shot noise in photon counting. Fluorescence polarization analysis has long been applied to the study of two-dimensional single-molecular motion in terms of φ[3–7]. This technique was subsequently extended to tracking three-dimensional motions of the lever arm domain of myosin V labeled with a bifunctional rhodamine, in terms of both θ and φ, using a time-multiplexing excitation protocol, to show that this 24-nm-long domain undergoes a swinging motion as large as ~80°, which corresponds to its motor domain traversing 36 nm along an actin filament[8]. In this and subsequent studies[9], four or eight linearly polarized excitations were used, with each of the resulting emissions split into two polarized emission components. Sixteen polarization signals allow unambiguous determination of orientation within a full hemisphere, which is required to measure large angle changes but may not be necessary in the case of small angle changes. The standard deviation (σ, commonly used as a measure of precision) of the distributions of θ and φ were reported as 10° and 14°, respectively, when the measurements comprised a few hundred photons captured from eight polarization channels during a sampling interval on the order of tens of milliseconds[8, 10, 11]. In comparison, the theoretical shot-noise-limited σ values of θ and φ are 6° and 10°, respectively[11]. In contrast, σ of 2 to 12° has been achieved in imaging-analysis studies of individual fluorophore molecules (not attached to protein), which required analyzing several thousand photons under conditions that minimized motions of fluorophores[12, 13].

Here we aimed to achieve an effective σ of 5° or less to resolve multi-state protein-conformational changes on angstrom and millisecond scales. As a test protein, we chose the cytosolic regulatory module of the prokaryotic Ca^{2+}-dependent K^+ channel MthK[14, 15]. The regulatory module controls the transmembrane channel pore, and is structurally four-fold symmetric around the central axis of the pore, comprising two stacked rings, each formed by four RCK (regulator of conductance to K^+) domains (Fig. 1b). An RCK domain can bind Ca^{2+}, and has a molecular weight of 25 kDa, compared to the average value of ~50 kDa for proteins. Crystallographic studies have captured three structural conformations of the RCK domain, dubbed S_1, S_2, and S_3 (Fig. 1c). The S_2 conformation was observed in a full MthK channel (PDB 1LNQ)[14], whereas S_1, either in a pure form (PDB 4RO0) or in a mixture with S_3 (PDB 2FY8)[15], was observed with the isolated regulatory module. When the three

conformations are aligned for a single RCK domain using the CNS program[16], the locations of individual backbone atoms differ by 0.2 Å to 9.2 Å. Thus, a single RCK domain within the regulatory module is an ideal system to develop a strategy for simultaneously achieving the high spatial and temporal resolutions required to examine conformational changes in a typical protein.

Results

Labeling, attaching and orientating protein molecules

We chose to track helix αB in the RCK domain because it is the closest to the channel gate formed by the second membrane-spanning segment (M2) in the pore module (Fig. 1b)[14, 15]. From the available crystal structures (PDB 1LNQ and 2FY8), this α-helix is expected to rotate by 10° to 16° among the three conformations, whereas its middle point, ~20 Å from a reference origin, is expected to move 3.4 to 8.1 Å angstroms (Fig. 1c). Residues E146 and L153 in the helix were replaced by two cysteine residues for attaching a bifunctional rhodamine molecule (Fig. 1a,b; Methods). The two-point attachment ensures alignment of the fluorophore with the helix, such that its dipole orientation would report the helix orientation. To minimize the probability of having more than one Cys-mutation-containing RCK domain in each regulatory module formed by eight RCK domains, we co-transformed bacteria with wild-type and mutant cDNAs in a 15:1 ratio. In addition, labeling of the purified RCK octamers was performed at a ratio of 1.8 : 1 bifunctional rhodamine to RCK, to further reduce the chance of having individual octamers labeled with more than one rhodamine molecule. We observed ~10% of fluorescent particles bleached in more than one step and excluded them from further analysis.

To attach the sample protein to a glass coverslip conjugated with streptavidin, we covalently linked biotin to its N-termini. The strong streptavidin-biotin interaction was exploited to create a stable attachment between the sample protein and the coverslip. An RCK octamer presents two indistinguishable faces normal to the four-fold axis, with four N-termini exposed on either face (Fig. 1b). A four-fold attachment between a ring of four RCK domains to the coverslip aligned the regulatory module's central axis with the z-axis, allowing us to group θ of each given conformational state determined from numerous molecules into a single distribution. From the resulting individual distributions of θ, we calculated the means and used them as a set of benchmarks to relate to the structures of the crystallographic states[14, 15] (Fig. 1b,c). The angle φ of the α-helix, relative to the x-axis, lies in the plane of the microscope slide (Fig. 1a,b). Because any given regulatory module should be randomly oriented relative to the x-axis, its φ value would also vary randomly across different complexes, yet the difference in φ between two states should remain the same statistically. Given that the angle change between two conformations in the actual rotation plane (Ω; Fig. 1c), reflects the change in φ and θ, we used Ω values among the three conformations as an additional set of benchmarks.

Specifications and optimization of the microscope

We used a polarization microscope equipped with a single laser, circularly polarized, to excite fluorophores under a total internal reflection condition, and two polarizing beam

splitters to separate fluorescence emission[17], which were recorded with an electron-multiplying charge-coupled device (EMCCD) camera (Methods and Supplementary Note 2). This approach was useful in previous studies of proteins labeled with very bright fluorescent nanoparticles[18, 19], yielding reasonable precision of angle measurement (σ of 12° for φ[18]). Here, an effective σ of ~5° or less is required to resolve the predicted 10 – 16° orientation changes in RCK labeled with rhodamine, which emits far fewer photons per second under the present experimental conditions. Polarizing beam splitters are critical determinants of the microscope's quality of polarization. Below, we use an idealized system to explain the imperfection of the splitters and necessary corrections for this and other imperfections (see Supplementary Notes 3 and 4 for more details).

A fluorophore can be modeled as a dipole that anisotropically emits photons; the orientation of its net electric field vector **E** can be defined by θ, φ and |**E**|, or equivalently by the three Cartesian components E_x, E_y and E_z.

$$\begin{aligned} E_{\mathrm{x}} &= |\mathbf{E}| \sin\theta \cos\varphi \\ E_{\mathrm{y}} &= |\mathbf{E}| \sin\theta \sin\varphi \\ E_{\mathrm{z}} &= |\mathbf{E}| \cos\theta \end{aligned} \tag{1}$$

where |**E**| is the vector's magnitude, related to the total emitted fluorescent light by $I_{\mathrm{tot}} \propto |\mathbf{E}|^2$ If this light were entirely directed to pass through a 0°-90° polarizing beam splitter aligned with the x-y axes respectively, the intensities I_{x} and I_{y}, which correspond to the E_{x} and E_{y} components, would be separated into the 0° and 90° polarization channels, respectively. I_{z} would be effectively indistinguishable by these polarization channels and therefore be split evenly between them. The intensities recorded in the 0° (I_0) channel would then be linear combinations of I_{x} and $\frac{1}{2}I_{\mathrm{z}}$, and the 90° ($I_{90}$) channel be that of I_{y} and $\frac{1}{2}I_{\mathrm{z}}$ (Supplementary Note 3). Thus, additional independent information is required to determine the dipole's orientation or its three electric-field components. If the intensity emitted from a fluorophore fixed in space were collected by one of h number of channels with a polarization angle of $\psi°$ (relative to the x-axis), the collected intensity (I_ψ) would be given by:

$$I_\psi(I_{\mathrm{tot}}, \theta, \varphi) = \frac{1}{h} I_{\mathrm{tot}} \left[\frac{1}{2} \sin^2\theta \cos 2(\varphi - \psi) + 1 \right] \tag{2}$$

where according to the dipole model, $I_{\mathrm{tot}} = 2|\mathbf{E}|^2$ (Supplementary Note 3). The sum of (I_ψ) over all channels would yield I_{tot}. As we could only split the beam into an even number of components, the three-dimensional information of **E** would be transformed to minimally four components, here I_0, I_{45}, I_{90}, and I_{135}, experimentally measurable in a two-dimensional space. In theory, determination of θ, φ, and I_{tot} requires measuring I_ψ from minimally three polarization channels[17]. However, in practice, the noise and depolarization of the four intensity recordings are expected to be different, and the four possible sets of angle calculations, each using three intensities, would lead to different numerical values. For achieving a unique set of calculated values, we derived from Eq. 2 the analytic expression for θ or φ, each of which is a function of all four intensities:

$$\varphi = \frac{1}{2}\tan^{-1}\frac{I_{45} - I_{135}}{I_0 - I_{90}} \quad (3)$$

$$\theta = \sin^{-1}\left[2\sqrt{\frac{\sqrt{(I_0 - I_{90})^2 + (I_{45} - I_{135})^2}}{(I_0 + I_{90} + I_{45} + I_{135})}}\right] \quad (4)$$

where either angle would be a function of an intensity ratio, and its resolution should thus be limited by the SNR of intensities; θ would be defined from 0° to 90° and φ from 0° to 180° with degenerate solutions of 180° - θ and 180° + φ, the degeneracy reflecting the underlying symmetry of the fluorophore dipole.

We initially used two Wollaston beam splitters as previously described[18] (Fig. 2a). Judging from the polarization ratio (dubbed f), the light passing through the 0°-90° splitter almost completely retained its original polarization (f_0 = 0.99 and f_{90} = 0.99), but only ~50% of the light remained polarized after passing through the 45°-135° splitter. This depolarization reduced the upper limit for the calculated θ to ~45° from the theoretical limit of 90°. To different degrees, the depolarizing effect was shared by all splitters that we tested for the 45°-135° configuration. Among them, a wire-grid polarizer yielded f_{45} = 0.85 and f_{135} = 0.79, which had been used previously[19]. With a Wollaston splitter (for 0°-90°) and a wire-grid polarizer (for 45°-135°), plus numerically correction of the depolarization, we restored θ to its full range. Additionally, the beam splitters would separate light into the polarized components according to the actual polarization angle ψ, which may significantly deviate from the expected value. Thus, only the calibrated ψ value should be used in the calculations (Methods and Supplementary Note 4). To account for the probe's diffusive motion and incomplete collection of photons by our microscope objective (with a 78.5° half angle (α) of the collection cone[20], as opposed to an α of 180° for full collection), we implemented additional, well-established corrections (Supplementary Note 3). Eqs. 53, 61 and 63 are the counterparts of Eqs. 2–4 with all above corrections (Supplementary Note 3). Using Eqs. 61 and 63, we calculated the angles to avoid any errors that might arise from failure to reach the global minimum during simultaneous fitting of multiple equations to a set of intensities, also markedly shortening the time to analyze the large number of data sets.

Recorded intensities and calculated angles

Using the EMCCD camera, we simultaneously captured components I_0, I_{45}, I_{90} and I_{135} of fluorescence emission from numerous spatially separated molecules (Fig. 2b). Fig. 3a shows consecutive sets of images of four polarized components from a single attached bifunctional rhodamine (Fig. 2b, boxed spot), recorded at a rate of 50 frames per second. For any given time point, the collected intensities completely defined θ and φ. From the simultaneous and relative variations in the four intensities, which reflect angle changes of the tracked helix, the underlying angstrom-scale intramolecular motions effectively became visually noticeable in real time (Fig. 3a; Supplementary Video 1).

We plotted the intensities of the four components of a fluorophore against time (Fig 3b), where each intensity value was a direct summation of individual pixels (Supplementary Note 2). Intensity I_{tot}, defined as the total emitted intensity, was calculated from the four recorded intensities with Eq. 62 (Supplementary Note 3). Furthermore, from the intensities of the four polarized components, we calculated θ and φ with Eqs. 63 and 61 (Supplementary Note 3), and plotted them in Fig. 3c, along with Ω calculated with Eq. 70 (Supplementary Note 6).

Event transition detection, state identification and angle resolution

We detected conformational transitions and identified states in two separate steps. We used the *changepoint* algorithm[21, 22] to detect event transitions on the basis of concurrent intensity changes, extracting temporal information. This method does not assume any specific kinetic model regarding the protein conformational changes; it simply detects event transitions by a likelihood ratio, i.e., testing two hypotheses (with 95% confidence) that, within a given time interval, an intensity change does or does not occur. A Gaussian filter was applied to all four intensity traces to reduce high-frequency noise in a manner that the shortest events, each comprising a single data point, retained more than half of their intensity values. Through calibration, we estimated that on average 55 photons (out of estimated ~120 emitted photons) were recorded from all four channels during each 20-ms exposure, where the signal-to-background ratio was ~10. Mean θ and φ were 56° and 90° whereas mean σ_θ and σ_φ were 8.6° and 9.1° (the fluorophore's wobble angle δ was set at 30°; Supplementary Note 5). To estimate the theoretical limits for σ_θ and σ_φ, we analyzed the variations of θ and φ, which were calculated from the intensities simulated for the above conditions, assuming those variations would arise solely from shot noise. The resulting theoretical limits of σ_θ and σ_φ yielded from this analysis were 8.0° and 6.4°, respectively. Thus, the precision of our angle measurements was close to being shot-noise limited.

Identification of transition points enabled us to average the data points within individual events, effectively increasing precision. Practically, from the original intensity I_ψ and angles (θ, φ, Ω) traces (Fig. 3b, c), we generated the corresponding black traces where the values of individual points within an event of a given trace were averaged over its lifetime. Following averaging (13 data points per event on average), the mean values of σ_θ and σ_φ were reduced to 4.2° and 4.4° on the basis of individual events, during which estimated 715 photons on average were collected from four channels. As further illustrated in Fig. 4a, in terms of SNR over a range of 3 to 13, the values of effective σ_θ and σ_φ ranged from 5° to 2°. Given that we tried to resolve angle changes as small as ~10°, we set effective σ values of ≤5° as a criterion for particle selection.

After intra-event data-point averaging, the distribution of θ exhibited three distinct peaks, whereas the distribution of φ exhibited only two peaks; the broader one likely reflected two unresolved peaks (Fig 3c). These characteristics are expected from the crystal structures where the θ value of the tracked α-helix differs among all three conformations by ≥10°, whereas its φ values for two conformations are within (unresolvable) 3°, each differing by ~10° from the third. For further illustration, we plotted θ against φ (Fig. 4b), color-coding individual data points according to the states, which were identified as described below. As

expected from the plot, the distribution of Ω, containing both θ and φ information, exhibited three distinct peaks (Fig. 3c).

We developed a program based on the *k*-means clustering algorithm[23] to identify conformational states from θ and φ together so as to increase resolvability and confidence. Following the examination of all possible cases, from one to four states (and more if necessary), the program determined the most probable number of states by comparing all examined cases using a F-test[24]. Of 980 particles analyzed, 85% exhibited three states, whereas the remaining particles exhibited a fourth state with the largest average θ of 85° (an example is shown in Fig. 3c, right side). The relative rarity of this fourth state makes it unreliable for further investigation, and we thus lumped those particles into the state with average θ of 75° while reanalyzing the relevant particles by assuming three states. The relative distributions of the three states, with or without those particles included, showed little difference.

Relating the identified conformational states to the crystal structures requires accurate angle values. To achieve greater accuracy of angle values, we determined mean θ and Ω values (Fig. 5) from the ensemble means of a large number of molecules already analyzed individually (as shown in Fig. 3c). In the three crystal structures, the θ values of the tracked α-helix range from 52° to 70°, and the Ω values range from 10 to 16° (Fig. 5). The ensemble means of the three θ and three Ω angles determined here were consistent with those determined from the crystal structures[14, 15] (Fig. 5). Although at the ensemble level, the mean angle values should be determined more accurately, the angle resolution would be poor. Indeed, the ensemble distributions built with angle values determined from molecule-by-molecule analyses (Fig. 5) shows a clear deterioration of resolution compared to that at the single-molecule level (Figs. 3c, 4), on the basis of the distribution width (defined by σ). Thus, the initial molecule-by-molecule data analysis, as shown in Fig. 3c, was essential to resolving individual angle states.

Among the three crystal structural states S_1, S_2 and S_3 of a given RCK domain in the regulatory module, the relative displacements of the α carbon of residue K150, which is located midway between E146C and L153C used to attach the fluorophore, are between 3.4 Å and 8.1 Å[14, 15]. These displacements should approximate those of the fluorophore's center. Thus, by resolving small angle changes, we have successfully detected conformational changes involving displacements on the order of angstroms.

Discussion

We showcased an application of a light microscope to quantitatively track the orientation changes of a fluorophore attached to a protein, which occur on a millisecond scale, by monitoring the changes in its emission anisotropy, with effective σ of 2° to 5°, or a mean of ~4° (Fig. 4a). The present method allows us to detect multi-state conformational changes in a single protein molecule and quantify the transitions in real time (50 frames per sec) among the conformational states that differ on an angstrom scale (Figs. 3 and 5; Supplementary Video 1).

As the angle resolution is limited by SNR of light intensity signals, we experimentally and analytically maximized effective SNR by the following means. First, we minimized the variance stemming from protein preparation and attachment. Second, we optimized the polarization microscope to achieve near shot-noise limited precision, and the expected full range of angle determination by using specific polarizing beam splitters and the implementation of a series of necessary numerical corrections. Third, by detecting the intensity change, we temporally demarcated individual events, extracting kinetic information. Fourth, the demarcation of individual events provided us the opportunity to average data points within a given event to mitigate the impact of noise, thereby increasing the resolution of individual events.

We emphasize that the purpose of the present method is to resolve, in real time, individual conformations of a protein, not to determine its atomic structures. This method has two fundamental requirements. First, following successful attachment, the fluorescent label must produce recordable polarized emission with SNR adequate for required resolution. Second, the changes in orientations of the label must report those of the individual conformational states.

In the two following papers, we demonstrate that the present approach enables the investigation of complex mechanisms underlying the protein's conformational changes and how the resulting dynamic information can be used as a temporal template to link existing structures of the protein[25, 26].

Online Methods

Production of recombinant isolated regulatory-module protein of MthK

The cDNA of RCK of the MthK channel from *Methanobacterium* thermoautotrophicum[14] (A0A090I3E9) was cloned into a pET28c vector containing a kanamycin-resistance gene. A 14-residue-long sequence was added to the N-terminus for recognition by biotin ligase, and a 6-His-tag was added to the C-terminus for affinity purification, with an intervening thrombin cutting sequence for removing the His-tag. We mutated Glu146 and Leu153, in the surface-exposed helix αB, to cysteines for covalent attachment of bifunctional rhodamine, while leaving the three endogenous, buried cysteine residues in place. Mutagenesis was performed using a PCR-based method and verified by DNA sequencing.

The RCK protein was expressed in *E. coli* BL-21 cells. To maximize the chances of having only one cysteine-mutation-containing RCK per regulatory module, BL21cells were transformed with a 15 : 1 ratio of wild-type and mutant cDNAs. Transformed BL-21 cell were grown in 2L LB with Kanamycin (50 μg/ml; American Bio AB01100) in a shaker incubator (37 °C). Protein expression was induced with Iso-propyl β-D-thiogalactopyranoside (IPTG) (0.4 mM; American Bio AB00841) at OD_{600} = 0.8 over 12–16 hours at 21 °C. Cells were then harvested and lysed using a French press in a solution containing 250 mM KCl and 10% glycerol, buffered at pH 8.0 with 10 mM Tris. To prevent proteolysis, a cocktail of protease inhibitors, "Complete" tablet (Sigma) plus phenylmethanesulfonyl fluoride (PMSF) (1 mM; Sigma P-7626), were added to the solution. The lysate was centrifuged, and the resulting supernatant was loaded onto a cobalt-resin

column pre-equilibrated with a solution containing 250 mM KCl, 10 mM imidazole, 10 mM Tris at pH 8.0. The protein was eluted from the column with a solution containing 250 mM KCl, 400 mM Imidazole, 10 mM Tris at pH 8.0. The eluted fractions containing the protein were pooled and treated with thrombin (0.8 units of per mg) to remove the His-tag on a gentle rocker at room temperature overnight. The protein sample was then concentrated using an MWCO Amicon Ultra concentrator with a molecular-weight-cutoff of 10,000 Daltons to a final volume of ~0.5 ml, before loading onto a Superdex-200 gel filtration FPLC column equilibrated in a solution containing 250 mM KCl, and 10 mM Tris titrated to pH 8.0.

Labeling of protein with bifunctional rhodamine and biotin

Attachment of bifunctional rhodamine (Bis-((N-Iodoacetyl)-Piperazinyl)-Sulfonerhodamine; Invitrogen B10621) with two iodoacetamide groups to E146C and L153C in the regulatory module and N-terminal biotinylation were performed following a previously described protocol with some modifications[8]. The protein sample in the gel filtration buffer at an ~50 μM concentration was treated with 50 μM reducing agent TCEP (Sigma T2556) at room temperature for one hour, after which 30 μM bifunctional rhodamine was added four times at 12-minute intervals. 54 minutes after the fourth addition, the labeling reaction was terminated with 3 mM MESNA (Sigma-Aldrich, M1511). As high concentration of K^+ inhibits the biotin ligase (BiRA; Avidity), the above protein sample was diluted 2.5 times with a solution containing 100 mM NaCl, and 2 mM EDTA titrated to pH 8.0, lowering the K^+ concentration to 100 mM. After adding a manufacturer-supplied reaction mix and BiRA (40 μg per 10 nmoles of sample protein), the biotin ligation reaction proceeded for 1 hour at 30 °C. To remove free biotin and bifunctional rhodamine and to raise KCl back to 250 mM KCl, the sample was dialyzed overnight in a 7000 MWCO Slide-A-lyzer (ThermoFisher 66373) against a solution containing 250 mM KCl and 10 mM Tris titrated to pH 8.0, in a 1:1000 volume ratio.

Fluorescence polarization microscope and intensity recording

We built the fluorescence polarized microscope from a Nikon microscope (model Ti-E). To produce an evanescent field at the surface of the sample coverslip, a linearly polarized laser beam (532 nm) generated from a 100 mW laser (Crystalaser CL532–100-S) was directed to pass through a ¼ λ-plate, which transformed the linear polarization to circular polarization. After passing through a 100X objective (Nikon Achromatic, NA = 1.49), the beam emerged at a 78° angle incident to the coverslip, the so-called critical angle that leads to TIR required for the formation of an evanescent field[27]. The emission of polarized fluorescent light from individual fluorophores excited by the evanescent field was directed to a 50:50 non-polarizing beam splitter (Thorlabs CM1-BS013) after passing through the objective, and a 540/593 nm bandpass filter (Semrock FF01–593/40–25) that prevents the propagation of excitation light. One resulting beam was further split by a Wollaston polarizing beam splitter (Edmund Optics 68820) along 0° and 90° and the other by a wire-grid polarizing beam splitter (Thorlabs WP25M-Vis) along 45° and 135° (Fig. 2a). These 4 beams, labeled as I_0, I_{45}, I_{90} and I_{135}, were individually directed onto 4 designated sectors in the CCD grid of an EMCCD camera (Andor iXon Ultra 897), where the four intensities from a given fluorophore appeared in the corresponding positions of the four sections (Fig. 2b).

For recording, the isolated regulatory module molecules labeled with biotin were attached to the sample coverslip with a high surface density of streptavidin covalently linked to the silica glass (customized by Arrayit), and covered in a solution containing 200 mM KCl, and 10 mM HEPES titrated to pH 8.0, where 1 mM EGTA was used as a buffer to achieve a nominally Ca^{2+}free condition. Just prior to a recording, 100 mM dithiothreitol (DTT) (Fisher, BP172) was added to scavenge oxygen to minimize its adverse impact on the fluorophore's emitting intensity and lifetime. Fluorescence intensities from individual bifunctional rhodamine molecules, each attached to an isolated regulatory-module molecule, were collected with the microscope and captured with the EMCCD camera. Following extraction of temporal information from the intensities with the *changepoint* analysis described below, we applied a Gaussian filter (with a corner frequency of 7.5 Hz) to all four intensity traces to reduce high-frequency noise, where the rise time was 44 ms. From these filtered intensities, we calculated angles as described in the text and Supplementary Note 3. When θ is near 90°, the noise of intensities might prevent a solution of θ, in which case we simply set the θ values to 90°. We only analyzed data from the particles with no more than a few percent of such data points.

Detection of event transitions

To detect event transitions within the measured polarized intensities, we adopted the *changepoint* algorithm[21]. This was based on calculating a log likelihood ratio over a period of time to determine the maximal ratio that identified the point where the change of photon-release rate occurred, i.e. where one event transitioned to another. This method has previously been applied to analyzing the photon-arrival time captured through multi-channel recordings[22]. Here we adapted it for analyzing the data collected over a fixed time interval with an EMCCD camera.

The photon release rate, i.e. intensity, changes when one event transitions to another (Supplementary Fig. 1a,b). When a camera is used as a detector, photons emerging from each channel are effectively binned over each frame. A series of consecutive k frames with a constant exposure time (Δt) is expressed as:

$$t_0,\ t_1,\ \ldots,\ t_{\mathrm{i}},\ t_{\mathrm{i}+1},\ \ldots,\ t_{\mathrm{m}-1},\ t_{\mathrm{m}} = 0,\ \Delta t,\ \ldots,\ i\,\Delta t,\ (i+1)\,\Delta t,\ \ldots,\ (k-1)\,\Delta t,\ k\,\Delta t \tag{5}$$

For a given frame i, the intensity I_{i} is defined by the rate of photon release:

$$I_{\mathrm{i}} = \frac{n_{\mathrm{i}}}{\Delta t} \tag{6}$$

where n_{i} is the number of photons release within frame i. The cumulative distribution, m_{j}, is built by adding the number of photons for the successive time frames:

$$m_{\mathrm{j}} = \sum_{\mathrm{i}=0}^{\mathrm{j}} n_{\mathrm{i}} \tag{7}$$

The slope (i.e., derivative) of the plot of m_{i} against i reflects the rate of photon release (Supplementary Fig. 1c). In theory, a transition occurs at the frame where the slope

significantly changes. Qualitatively, slope changes, which result from relative photon release rates among the four polarization channels, should occur at the same frame for all channels; this redundancy increases the reliability of transition detection (Supplementary Fig. 1b, c). On the cumulative distribution plot of the logarithmic (*log*) *likelihood* for all four intensities together, the transition point occurs at a distinct maximum (Supplementary Fig. 1d), which forms the basis of automated detection.

Theoretically, for a given frame i, the probability p_i of collecting n_i number of photons, emitted at an average rate $I = \langle n \rangle / \Delta t$, is given by the Poisson distribution:

$$p_i = (I\Delta t)^{n_i} e^{-I\Delta t} \tag{8}$$

The likelihood (L_0) of the fluorophore emitting photons at this rate over all frames ($i = 0 \ldots F$) is given by:

$$L_0 = \prod_{i=1}^{F} p_i = \prod_{i=1}^{F} \frac{1}{n_i!} (I\Delta t)^{n_i} e^{-I\Delta t} \tag{9}$$

The log likelihood (LL) of L_0 is then:

$$\begin{aligned} LL_0 &= \ln \prod_{i=1}^{F} p_i = \sum_{i=1}^{F} \left[n_i (\ln(\Delta t) - 1) - \ln(n_i!) \right] = N \ln\left(\frac{N}{T}\right) \\ &+ N(\ln(\Delta t) - 1) - \sum_{i=1}^{F} \ln(n_i!) \end{aligned} \tag{10}$$

where $N = \sum_{i=1}^{F} n_i$ is the total number of photons emitted over time $T = F\Delta t$. If during the interval T the rate changes from I_1 to I_2 at the time point $\tau = f\Delta t$, and the number of emitted photons prior to this change is $m = \sum_{i=1}^{f} n_i$, and after the change it is $N - m$, then the function describing the likelihood of a transition to occur at frame f in the log form is:

$$\begin{aligned} LL_1 &= \ln\left(\prod_{j=1}^{f} p(I_{1_j}) \prod_{k=f}^{F} p(I_{2_k}) \right) = m \ln(I_1) + (N - m) \ln(I_2) \\ &+ N(\ln(\Delta t) - 1) - \sum_{i=1}^{F} \ln(n_i!) \end{aligned} \tag{11}$$

A relation for comparing the two cases is given by their log likelihood ratio, i.e. $LL_R = LL_1 / LL_0$:

$$\begin{aligned} LL_R &= \ln\left(\frac{\prod_{j=1}^{f} p(I_{1j}) \prod_{k=f}^{F} p(I_{2_k})}{\prod_{i=1}^{F} p(I_i)} \right) = m \ln\left(\frac{m}{\tau}\right) + (N - m) \ln\left(\frac{N - m}{T - \tau}\right) \\ &- N \ln\left(\frac{N}{T}\right) \end{aligned} \tag{12}$$

This ratio operation eliminates Δt, and LL_R is thus independent of Δt.

Further, to increase the reliability of the detection, we combined the likelihood function for each channel (1…*h*) to give a combined log-likelihood-ratio function:

$$LL_{\mathrm{R}} = \ln\left(\prod_{\mathrm{r}=1}^{\mathrm{h}} \frac{\prod_{\mathrm{j}=1}^{\mathrm{f}} \mathrm{p}\left(I_{1_{\mathrm{j,r}}}\right) \prod_{\mathrm{k}=\mathrm{f}}^{\mathrm{F}} \mathrm{p}\left(I_{2_{\mathrm{k,r}}}\right)}{\prod_{\mathrm{i}=1}^{\mathrm{F}} \mathrm{p}\left(I_{\mathrm{i,r}}\right)}\right) \quad (13)$$

Substituting Eq. 8 into Eq. 13 yields:

$$LL_{\mathrm{R}} = \sum_{\mathrm{r}=1}^{\mathrm{h}} m_{\mathrm{r}} \ln\left(\frac{m_{\mathrm{r}}}{\tau}\right) + \left(N_{\mathrm{r}} - m_{\mathrm{r}}\right) \ln\left(\frac{N_{\mathrm{r}} - m_{\mathrm{r}}}{T - \tau}\right) - N_{\mathrm{r}} \ln\left(\frac{N_{\mathrm{r}}}{\mathrm{T}}\right) \quad (14)$$

We set the threshold of significance for LL_R at the level that limits the false positive events to 5% on the basis of simulation studies, and the resulting false negative events were about 1%.

The program started by identifying one transition over the entire trace. If a change-point X was identified, it would then search for additional transitions between the start of the trace and point X and between X and the end. This iterative search with successively shortened stretches continued until no more transitions were identified.

State identification

We calculated θ and φ with Eqs. 63 and 61 (Supplementary Note 3), and identified multiple states that occurred concurrently in both angle traces, using a *k*-Means clustering algorithm, which assumed values in each of *k* number of states followed a Gaussian distribution[23]. The algorithm operated on a 'nearest neighbor' principle where each data point was assigned to one of *k* distributions such that the mean value μ_{k} of the distribution had the shortest distance (d_{k}) to that of the interrogated data point (Supplementary Fig. 2). In terms of θ and φ of each event, such a distance was calculated between data point x_{i} and μ_{k} as:

$$d_{\mathrm{i,k}} = \sqrt{\left({}_{\theta}\mu_{\mathrm{k}} - {}_{\theta}x_{\mathrm{i}}\right)^2 + \left({}_{\varphi}\mu_{\mathrm{k}} - {}_{\varphi}x_{\mathrm{i}}\right)^2} \quad (15)$$

This process was first performed against initial guess values of distribution means. The distance $d_{\mathrm{i,k}}$ was then recalculated and reassigned to the compared distributions on the basis of the resulting means. The process was repeated until there were no further re-assignments. This algorithm itself offered a simple and adequate means to sort data against two states. However, in the case of multiple states, a *k*-Means clustering algorithm was highly sensitive to initial guess values and proved to be extremely challenging, if not practically impossible without being coupled to adequate optimization algorithms. As such, we used a Nelder-Mead downhill simplex routine coupled to a simulated annealing routine[23] to optimize the state identification program, which was based on a *k*-Means clustering algorithm, in the form of the ratio of log likelihood functions:

$$LL_1 = \sum_i \left[\left({}_{\theta}\mu_1 - {}_{\theta}x_{\mathrm{i}}\right)^2 + \left({}_{\varphi}\mu_1 - {}_{\varphi}x_{\mathrm{i}}\right)^2\right] \quad (16)$$

for the case of one state and:

$$LL_{\mathrm{k}} = \sum_{\mathrm{k}} \sum_{\mathrm{i}} \left[\left({}_{\theta}\mu_{\mathrm{k}} - {}_{\theta}x_{\mathrm{i}} \right)^2 + \left({}_{\varphi}\mu_{\mathrm{k}} - {}_{\varphi}x_{\mathrm{i}} \right)^2 \right] \tag{17}$$

for the case of k number of states. The ratio of these two functions is given by:

$$LL_{\mathrm{R}} = \frac{LL_{\mathrm{k}}}{LL_{1}} = \frac{\sum_{\mathrm{k}} \sum_{\mathrm{i}} \left[\left({}_{\theta}\mu_{\mathrm{k}} - {}_{\theta}x_{\mathrm{i}} \right)^2 + \left({}_{\varphi}\mu_{\mathrm{k}} - {}_{\varphi}x_{\mathrm{i}} \right)^2 \right]}{\sum_{\mathrm{i}} \left[\left({}_{\theta}\mu_{1} - {}_{\theta}x_{\mathrm{i}} \right)^2 + \left({}_{\varphi}\mu_{1} - {}_{\varphi}x_{\mathrm{i}} \right)^2 \right]} \tag{18}$$

Application of the *k*-Means clustering algorithm coupled with the two optimization routines identified the most probable distribution to which each data point belonged, as shown in Supplementary Fig. 2. We have tested this state identification process with series of simulated traces where two states were separated by a varying fold of the standard deviation σ.

To assess the most probable number of states, we analyzed each set of data, as described above, in the framework of the models assuming a varying number of states, $k = 1, 2 \ldots n$. These models would be nested such that their differences should solely result from a different number of states. We thus judged whether one model of k states was more compatible with the data than another model of k+1 states by performing a F-test to determine (with a 95% confidence), on the basis of the statistical difference between the respective Chi-squared values (X^2_{k} to $X^2_{\mathrm{k+1}}$)[24] calculated with Eq. 17. Thus, as a whole, the entire state identification program encompassed a *k*-Means clustering algorithm, two optimization routines, and statistical evaluation of X^2 functions with a F test[24].

Code Availability

Code used in the work will be made available upon reasonable request.

Data availability

Data and materials described here will be made available upon reasonable request.

Supplementary Material

Refer to Web version on PubMed Central for supplementary material.

Acknowledgments

We thank Y. Zhou for technical assistance; Y. Goldman for inspiration and the use of microscopes in his laboratory to test our initial fluorescence-labeled protein samples; Y. Jiang and R. MacKinnon for providing the cDNA encoding MthK; L. Lippert and T. Dadosh for discussions; P. De Weer; T. Hoshi and B. Salzberg for critiques of our manuscript at different stages of its development; and E. McCleskey for support. This study was supported by the grant GM055560 from the National Institute of General Medical Sciences of the National Institutes of Health to Z.L. During the initial period of the project, Z.L. was supported as an investigator by the Howard Hughes Medical Institute.

References

1. Brocchieri L, Karlin S Protein length in eukaryotic and prokaryotic proteomes. Nucleic Acids Res. 33, 3390–3400 (2005). [PubMed: 15951512]
2. Erickson HP Size and shape of protein molecules at the nanometer level determined by sedimentation, gel filtration, and electron miscroscopy in Biological Procedures Online (ed. Li S) 32–51 (Springer, 2009).
3. Sase I, Miyata H, Ishiwata S, & Kinosita K Jr. Axial rotation of sliding actin filaments revealed by single-fluorophore imaging. Proc. Natl. Acad. Sci. U. S. A 94, 5646–5650 (1997). [PubMed: 9159126]
4. Warshaw DM et al. Myosin conformational states determined by single fluorophore polarization. Proc. Natl. Acad. Sci. U. S. A 95, 8034–8039 (1998). [PubMed: 9653135]
5. Ha T, Glass J, Enderle T, Chemla DS, & Weiss S Hindered rotational diffusion and rotational jumps of single molecules. Physical Review Letters 80, 2093–2096 (1998).
6. Adachi K et al. Stepping rotation of F1-ATPase visualized through angle-resolved single-fluorophore imaging. Proc. Natl. Acad. Sci. U. S. A 97, 7243–7247 (2000). [PubMed: 10840052]
7. Sosa H, Peterman EJ, Moerner WE, & Goldstein LS ADP-induced rocking of the kinesin motor domain revealed by single-molecule fluorescence polarization microscopy. Nat. Struct. Biol 8, 540–544 (2001). [PubMed: 11373624]
8. Forkey JN, Quinlan ME, Shaw MA, Corrie JE, & Goldman YE Three-dimensional structural dynamics of myosin V by single-molecule fluorescence polarization. Nature 422, 399–404 (2003). [PubMed: 12660775]
9. Beausang Schroeder, H.W., Nelson, P.C., & Goldman, Y.E. Twirling of actin by myosins II and V observed via polarized TIRF in a modified gliding assay. Biophysical Journal 95, 5820–5831 (2008). [PubMed: 18931255]
10. Rosenberg SA, Quinlan ME, Forkey JN, & Goldman YE Rotational motions of macro-molecules by single-molecule fluorescence microscopy. Acc. Chem. Res 38, 583–593 (2005). [PubMed: 16028893]
11. Forkey JN, Quinlan ME, & Goldman YE Measurement of single macromolecule orientation by total internal reflection fluorescence polarization microscopy. Biophys. J 89, 1261–1271 (2005). [PubMed: 15894632]
12. Backlund MP et al. Simultaneous, accurate measurement of the 3D position and orientation of single molecules. Proc. Natl. Acad. Sci. U. S. A 109, 19087–19092 (2012). [PubMed: 23129640]
13. Zhang O, Liu J, Ding T, & Lew M Imaging the three-dimensional orientation and rotational mobility of fluorescent emitters using the Tri-spot point spread function. Applied Physics Letters 113, 031103, (2018). [PubMed: 30057423]
14. Jiang Y et al. Crystal structure and mechanism of a calcium-gated potassium channel. Nature 417, 515–522 (2002). [PubMed: 12037559]
15. Ye S, Li Y, Chen L, & Jiang Y Crystal structures of a ligand-free MthK gating ring: insights into the ligand gating mechanism of K^+ channels. Cell 126, 1161–1173 (2006). [PubMed: 16990139]
16. Brunger AT et al. Crystallography & NMR system: A new software suite for macromolecular structure determination. Acta Crystallogr. D. Biol. Crystallogr 54, 905–921 (1998). [PubMed: 9757107]
17. Fourkas JT Rapid determination of the three-dimensional orientation of single molecules. Optics Letters 26, 211–213 (2001). [PubMed: 18033550]
18. Ohmachi M et al. Fluorescence microscopy for simultaneous observation of 3D orientation and movement and its application to quantum rod-tagged myosin V. Proc. Natl. Acad. Sci. U. S. A 109, 5294–5298 (2012). [PubMed: 22431610]
19. Lippert LG et al. Angular measurements of the dynein ring revaeal a stepping mechanism dependent on a flexible stalk. Proc. Natl. Acad. Sci. U. S. A 114, E4564–E4573 (2017). [PubMed: 28533393]
20. Axelrod D Carbocyanine dye orientation in red cell membrane studied by miscroscopic fluororescence polarization. Biophysical Journal 26, 557–574 (1979). [PubMed: 263688]

21. Chen J & Gupta AK On change point detection and estimation. Communications in Statistics-Simulation and Computation 30, 665–697 (2001).

22. Beausang JF, Goldman YE, & Nelson PC Changepoint analysis for single-molecule polarized total internal reflection fluorescence microscopy experiments. Methods Enzymol. 487, 431–463 (2011). [PubMed: 21187234]

23. Press WH, Teukolsky SA, Vetterling WT, & Flannery BP Numerical Recipes: The art of scientific computing (Cambridge University Press, New York, 2007).

24. Horn R Statistical methods for model discrimination. Applications to gating kinetics and permeation of the acetylcholine receptor channel. Biophys. J 51, 255–263 (1987). [PubMed: 2435330]

25. Lewis JH & Lu Z Energetics of angstrom-scale conformational changes in an RCK domain of the MthK K^+ channel. Nat. Struct. Mol. Biol 261, 808–815 (2019).

26. Lewis JH & Lu Z Integrating spatiotemporal features of a ligand-regulated, multi-state allosteric protein. Nat. Struct. Mol. Biol 261, 816–822 (2019).

27. Axelrod D Total internal reflection fluoroscence. Annu. Rev. Biophys. Bioeng 13, 247–268 (1984). [PubMed: 6378070]

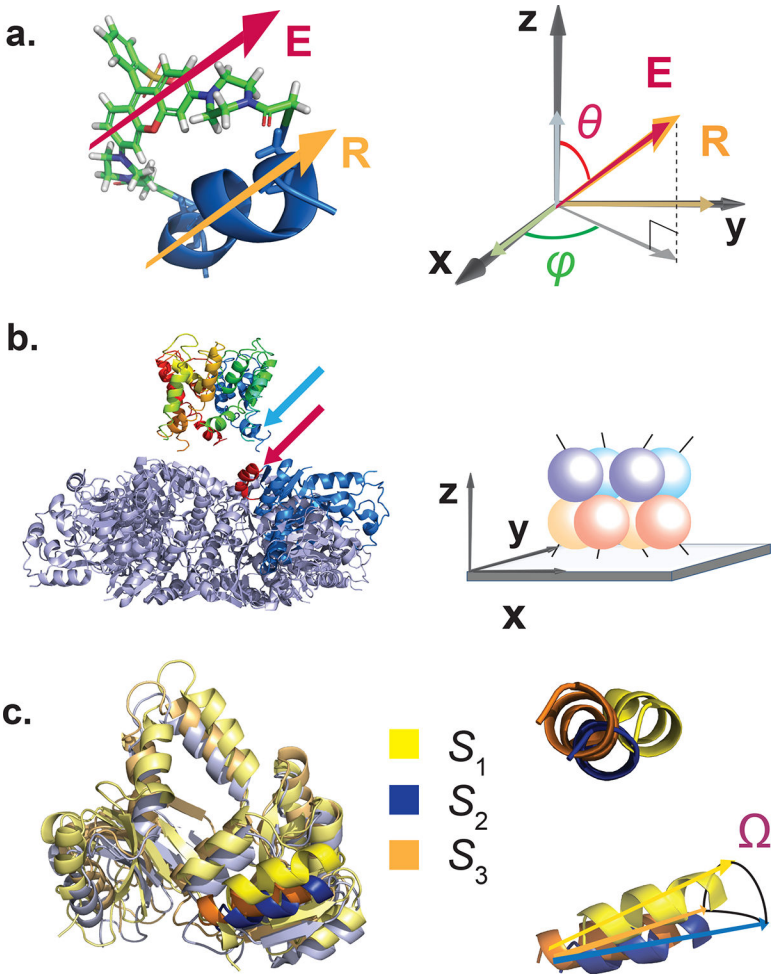

Figure 1.

Structural features of the MthK channel, and relationship between the spatial orientations of helix αB and the dipole electric field of a bifunctionally attached rhodamine. **a**. Left, chemical structure model of a rhodamine moiety attached to helix αB from the RCK domain (blue ribbon representation). Red arrow is a vector representing the rhodamine dipole electric field (**E**); orange arrow is a vector representing the α-helix (**R**). Right, vectors **E** and **R** can be defined in a single spherical coordinate system by a common pair of angles θ and φ, and their respective, differing magnitudes |**E**| and |**R**|. **b**. Left, crystal structure of the MthK channel (PDB 1LNQ)[14]. The transmembrane pore is at the top, with the helix forming the gate indicated with a cyan arrow; the cytosolic regulatory module is shown at the bottom, where one of the eight RCK domains is colored blue and helix αB chosen for rhodamine labeling is indicated with a red arrow. Right, cartoon of an isolated regulatory module anchored to a glass cover slip. Each sphere represents a single RCK domain, and the sticks represent the attached biotin moieties, which can interact with the streptavidin-coated cover slip. **c**. Left, alignment of the three RCK conformations, with helix αB colored yellow in S_1, blue in S_2 and orange in S_3 (PDBs: 1LNQ and 2FY8)[14, 15]. Right, the three conformations of helix αB are shown in two views; the color-coded arrows in the lower one are parallel to the respective helices. Ω is the angle between a given pair of arrows.

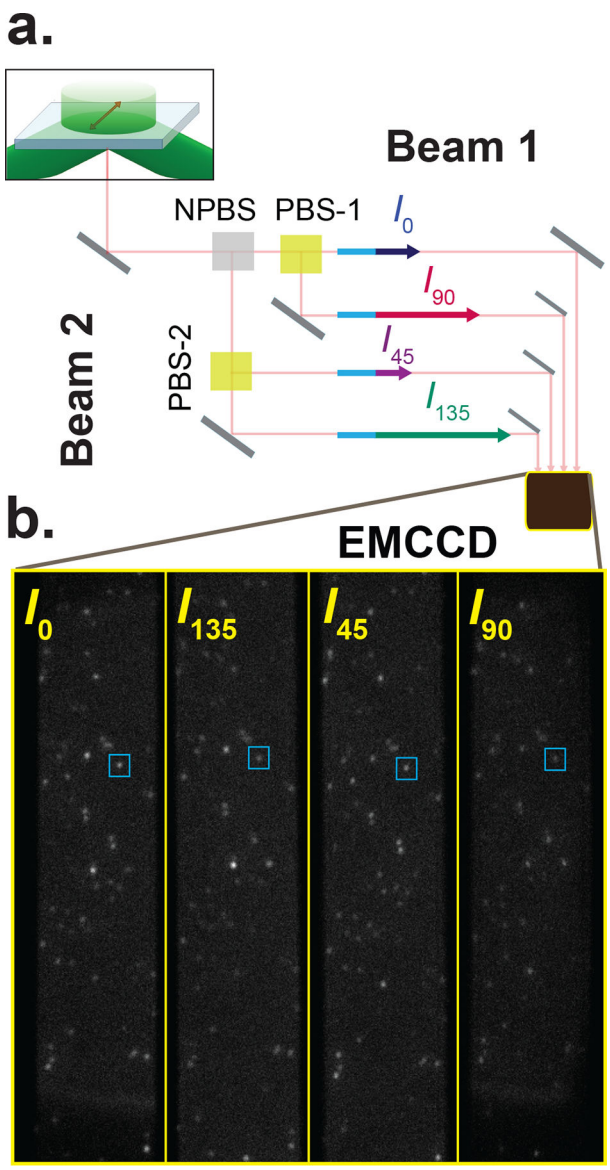

Figure 2.

Schematics of the microscope and splitting of fluorescence intensities. **a**. The dipole of a rhodamine-labeled particle, represented by the double-headed maroon arrow in the upper-left corner, is excited by a circularly polarized evanescent field represented by the green cylinder. Part of the polarized emission from the rhodamine's dipole propagates through the objective and is split evenly into beams 1 and 2 using a non-polarizing beam splitter (NPBS). Beam 1 is further split by a Wollaston polarizing beam splitter (PBS-1) into 0° (I_0) and 90° (I_{90}) polarized components, whereas beam 2 is split by a wire-grid polarizing beam splitter (PBS-2) into 45° (I_{45}) and 135° (I_{135}) components. Thick gray lines represent mirrors oriented at a 45° angle. The four colored arrows indicated the magnitude of the respective polarized component, relative to that of the non-polarized component indicated by a cyan line. **b**. Intensity for each of the four components (I_0, I_{45}, I_{90} and I_{135}) from

individual fluorescent particles captured by an EMCCD camera, with each component in a designated zone. The analysis of the particle in the blue box is shown in Fig. 3.

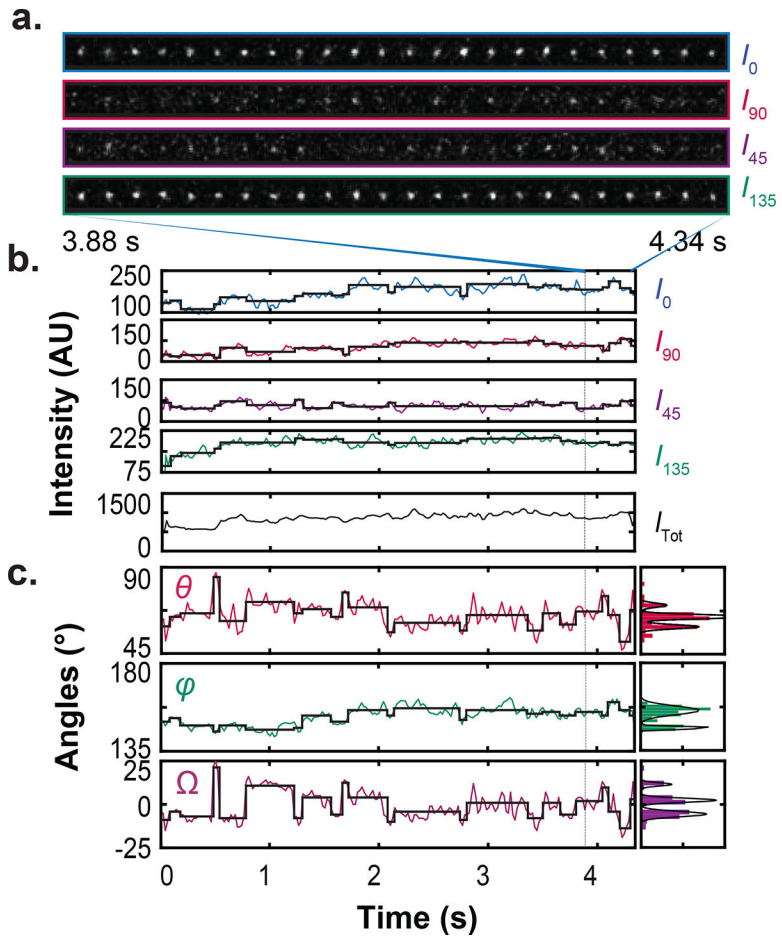

Figure 3.

Polarized-fluorescence intensities, and calculated θ, φ and Ω. **a**. Consecutive frames of four intensity components (I_0, I_{45}, I_{90} and I_{135}) of a fluorescent particle (boxed in blue, Fig. 2b) captured over the last 0.5 sec of an ~4-second recording (Supplementary Video 1). **b**. Intensity values of the four components, plotted against time, were integrated from 218 sets of consecutive images, part of which is shown in **a**; I_{tot} was calculated from I_0, I_{45}, I_{90} and I_{135} using Eq. 62 (Supplementary Note 3). **c**. Values of θ and φ were calculated from the four intensity components whereas the value of the angle change Ω, defined relative to S_2, was calculated using Eq. 70 (Supplementary Note 6). Transition points of the black traces superimposed on the records were determined by the *changepoint* analysis whereas the constant values between points were set to the means of the observed data points. Shown on the right are angle histograms generated from the black traces, superimposed with Gaussian fits.

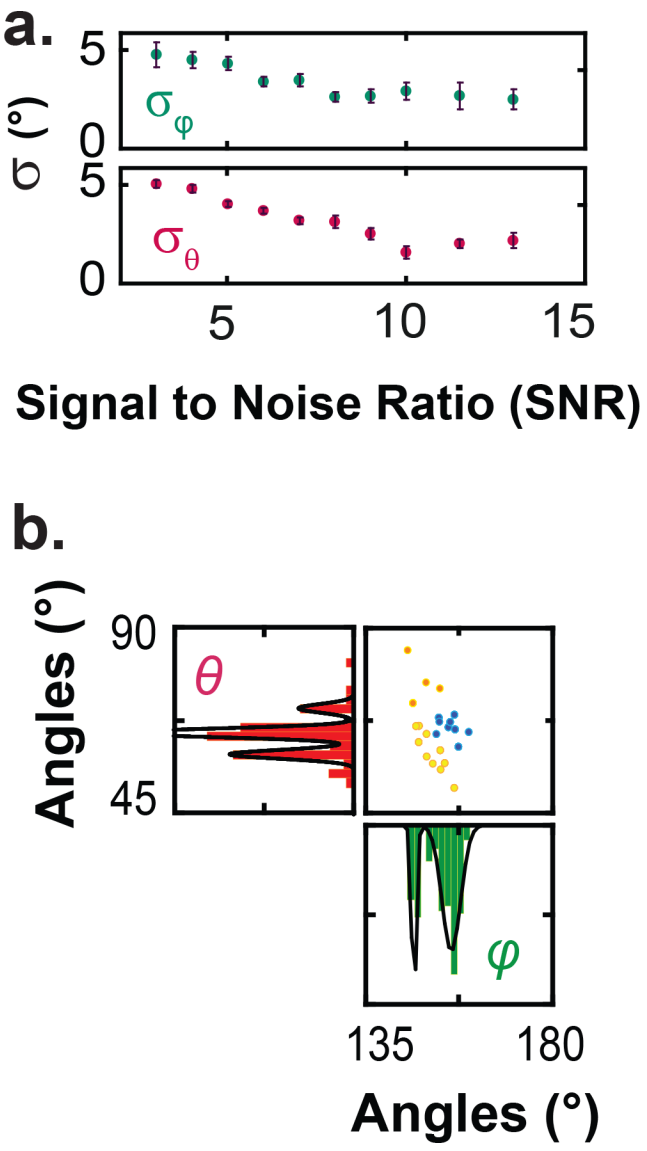

Figure 4.

Angle resolution and distributions obtained through single-particle analysis. **a**. σ_θ and σ_φ (mean ± s.e.m.) plotted against observed SNR, which were obtained from analyzing a pool of data collected in a range of Ca^{2+} concentrations[25, 26]. Each point encompasses the data that fall in the SNR range defined by the *x*-coordinate values of two consecutive points and is plotted at the position of the smaller value. Mean SNR for each data point was calculated on a per-intensity-channel basis and with the assumption of Gaussian noise, because other noise besides shot noise was likely also present. Number of particles for each SNR value: 3 (n=259), 4 (n=217), 5 (n=207), 6 (n=128), 7 (n=76), 8 (n=39), 9 (n=32), 10 (n=14), 11.5 (n=10) or 13 (n=4). **b**. Distributions of θ (red) and φ (green) of the particle taken from Fig. 3c, superimposed with Gaussian fits; top right, θ values of individual events plotted against their corresponding φ values. Data are color-coded according to state: S_1 (yellow), S_2 (blue) and S_3 (orange).

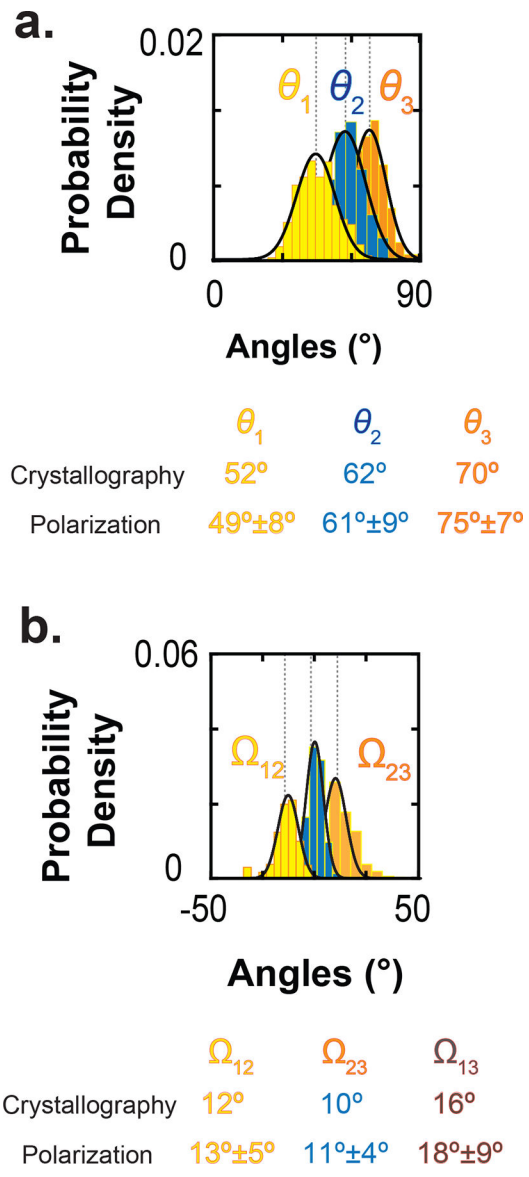

Figure 5.

Ensemble distributions of θ or Ω angles determined from fluorescence polarization measurements. **a, b**. Ensemble distributions of three θ (**a**) or Ω (**b**) angles constructed with data obtained from 316 rhodamine-labeled regulatory-module particles under nominal Ca^{2+}-free conditions, each of which was analyzed individually. Gaussian curves superimposed on the distributions were calculated with the mean and σ values of the respective angles. Below each distribution is the comparison of θ or Ω values (mean ± σ, calculated from data used to build the distribution) with those measured from the crystal structures of RCK in three states[14, 15].